ELSEVIER

Journal of Applied Geophysics 40 (1998) 105–116

JOURNAL OF APPLIED GEOPHYSICS

Radar attenuation tomography using the centroid frequency downshift method

Lanbo Liu [a,*], John W. Lane [b,1], Youli Quan [c,2]

[a] *Department of Geology and Geophysics, 354 Mansfield Road, U-45, University of Connecticut, Storrs, CT 06269-2045, USA*

[b] *Branch of Geophysical Applications and Support, U.S. Geological Survey, 11 Sherman Place, U-5015, Storrs, CT 06269, USA*

[c] *Department of Geophysics, Stanford University, Stanford, CA 94305, USA*

Received 3 February 1997; accepted 28 May 1998

Abstract

A method for tomographically estimating electromagnetic (EM) wave attenuation based on analysis of centroid frequency downshift (CFDS) of impulse radar signals is described and applied to cross-hole radar data. The method is based on a constant-*Q* model, which assumes a linear frequency dependence of attenuation for EM wave propagation above the transition frequency. The method uses the CFDS to construct the projection function. In comparison with other methods for estimating attenuation, the CFDS method is relatively insensitive to the effects of geometric spreading, instrument response, and antenna coupling and radiation pattern, but requires the data to be broadband so that the frequency shift and variance can be easily measured. The method is well-suited for difference tomography experiments using electrically conductive tracers. The CFDS method was tested using cross-hole radar data collected at the U.S. Geological Survey Fractured Rock Research Site at Mirror Lake, New Hampshire (NH) during a saline-tracer injection experiment. The attenuation-difference tomogram created with the CFDS method outlines the spatial distribution of saline tracer within the tomography plane.

Keywords: centroid frequency; borehole radar; attenuation tomography; saline injection

1. Introduction

Impulse radar methods utilizing the electromagnetic (EM) spectrum in the megahertz to gigahertz (MHz–GHz) frequency range are widely used to characterize near-surface structures. The methods have been applied from the surface and from boreholes to a wide range of hydrogeologic and engineering problems (Greenhouse, 1992; Greenhouse et al., 1993; Brewster and Annan, 1994; Brewster et al., 1995; Daniels et al., 1995; Sato et al., 1995; Grumman and Daniels, 1996; Versteeg et al., 1996; Liu et al., 1997). Radar methods can identify subsurface structures (i.e., bedding,

* Corresponding author. Tel.: +1-860-486-1388; Fax: +1-860-486-1383; E-mail: lanbo@geol.uconn.edu

[1] E-mail: jwlane@usgs.gov

[2] Current address. Exploration and Production Technology Department, Texaco, 3901 Briarpark, Houston, TX 77042, USA.

0926-9851/98/$19.00
PII: S0926-9851(98)00024-X

fractures, and buried utilities) that induce significant physical property contrasts (dielectric permittivity, electrical conductivity, or magnetic permeability). Interpretation of subtle contrasts in physical properties caused by changes in the fluid content within pore-spaces or fractures (i.e., non-aqueous phase liquids, or NAPL) is much more difficult. There are several reasons for the difficulty including: (1) changes in pore-fluid content generate relatively small contrasts in the effective physical properties; and (2) the heterogeneities caused by NAPL can be irregularly shaped, randomly distributed, and with smeared boundaries. These features result in weak reflection and transmission anomalies. Identifying the spatial distribution and quantifying the physical properties of anomalies in the subsurface would increase the likelihood of detecting subtle subsurface targets such as NAPL contamination.

It is possible to estimate the distribution of subsurface attenuation from EM wave absorption and dispersion to identify formation of physical properties (Sen et al., 1981; Feng and Sen, 1985; Endres and Knight, 1991; Endres and Redman, 1996). Measurements of both velocity and attenuation can provide complementary information about formation properties (e.g., Quan and Harris, 1993, 1997). For example, in seismic exploration studies, Brzostowski and McMechan (1992) used changes in seismic amplitudes to estimate attenuation distribution and determine the quality factor Q distribution.

Propagation of an EM pulse in a lossy medium broadens the pulse because of absorption and dispersion due to intrinsic attenuation, causing the amplitude of the pulse to decay. The rise-time associated with this broadening effect has been used to estimate attenuation (e.g., Kjartansson, 1979; Zucca et al., 1994). However, amplitudes are easily contaminated by factors such as scattering, geometric spreading, source and receiver coupling, radiation patterns, and transmission and reflection effects. It can be difficult to obtain reliable attenuation estimates from time-domain data. Therefore, we adapted a frequency–domain method developed by Quan and Harris (1993, 1997) for seismic data that uses the estimated shift in the centroid of the pulse spectrum as a quantity to estimate attenuation. To the first order, the frequency-shift or pulse-broadening of an EM pulse is not affected by far-field geometrical spreading or reflection losses, appears to be more reliable than the time-domain amplitude-decay methods, and can be easily implemented by a tomography algorithm.

The assumption that EM velocity and attenuation are independent of frequency is commonly used to simplify conventional radar processing and analysis. However, a noticeable downshift of the centroid frequency of a radar pulse is commonly observed in radar data. Because of this effect, receiver antennas with center frequencies lower than the transmitting antennas have been used in laboratory and field experiments to better match the spectrum of the received radar signals (Greeuw et al., 1992). The centroid frequency downshift (CFDS) is linked to attenuation (coupling absorption and dispersion) and can be attributed to dielectric losses. There are at least three mechanisms in dielectric losses: (1) the Debye effect, i.e., a binding effect of water to solid surfaces which decreases the dipolar relaxation frequency; (2) the Maxwell–Wagner effect, a texture effect enhanced by the presence of platy insulating particles; and (3) polarization of the double layer in the water near charged particles.

The CFDS method requires the data to be broadband to easily estimate shifts in the centroid frequency. This requirement is easily met by most commercial GPR and borehole radar systems. High attenuation is generally considered a major obstacle which is preventing the use of GPR in certain areas with high electric conductivity. The CFDS method presents an approach that could extend the operational range of GPR to include somewhat higher electrical conductivities by providing useful information on the distribution of subsurface attenuation. As a preliminary test, Liu and Quan (1996) applied

the CFDS method to surface GPR reflection data to derive the average formation attenuation between two subsurface layers. Use of the CFDS method with other processing and tomographic methods may help produce more accurate, stable subsurface images to identify physical property distribution in the subsurface. The method could be applied to a wide range of hydrogeologic, environmental, and engineering characterization problems.

The CFDS method is well-suited for difference-tomography experiments, which utilize an electrically conductive tracer to alter the attenuative properties of transmissive regions in the tomographic image plane. In this paper, we describe the CFDS method and demonstrate results of the method applied to cross-hole radar tomography data collected at the U.S. Geological Survey Fractured Rock Research Site at Mirror Lake, NH before and during a saline-tracer injection test in a fractured crystalline rock.

2. Electromagnetic wave attenuation

The attenuation, α, of EM waves transmitted in a lossy medium can be written as:

$$\alpha = \omega\left(\frac{\mu\varepsilon}{2}\right)^{1/2}\left[\left(1+\tan^2\delta\right)^{1/2}-1\right]^{1/2}, \qquad (1)$$

with $\tan\delta$, the loss tangent, defined as:

$$\tan\delta = \frac{\sigma}{\omega\varepsilon} = \frac{\omega_t}{\omega} = \frac{f_t}{f}, \qquad (2)$$

where: $\omega = 2\pi f$ is the angular frequency of the EM wave, in radian per second; f = frequency, in hertz or megahertz; μ = magnetic permeability, in henries per meter; ε = dielectric permittivity, in farads per meter; σ = electrical conductivity, in siemens per meter.

The ratio σ/ε defines the transition frequency, ω_t, and the ratio of the transition frequency and the signal frequency define the loss tangent (Annan, 1996). If the EM parameters of a material are independent of frequency, the transition frequency is constant. Discussion in this paper is confined to the wave propagation regime (above the transition frequency) in which impulse radar systems are designed to operate.

The quality factor, Q, is useful for characterizing wave attenuation (e.g., Sheriff and Geldart, 1995). The Q factor is defined as the ratio of total energy restored and the energy loss in one cycle and can be written as:

$$Q = \frac{\omega}{2c\alpha}, \qquad (3)$$

where: $(c = 1/\sqrt{\mu\varepsilon})$ is the phase velocity, in meters per second.

For EM wave propagation, when the loss tangent (Eq. (2)) is relatively small, Eq. (1) can be approximated (Balanis, 1989) by:

$$\alpha = \omega\sqrt{\mu\varepsilon}\left(\frac{1}{2}\tan\delta\right) = \frac{\omega}{2c}\tan\delta, \qquad (4)$$

where we used the relation between phase velocity and physical parameters $(c = 1/\sqrt{\mu\varepsilon})$ for electromagnetic waves. The loss tangent is related to the Q factor by:

$$\tan\delta = \frac{1}{Q}. \qquad (5)$$

A small loss tangent corresponds to relatively large Q value, which implies that the energy loss in one single cycle is small. For seismic waves, Q is relatively frequency-independent over a large frequency range (Kjartansson, 1979). Although there are seismic attenuation mechanisms which have some frequency dependences, the combined effect of individual mechanisms produces attenuation described by a constant Q model that is nearly linear with frequency.

Laboratory measurements show that the attenuation of radar waves over the bandwidths of typical radar pulses propagating in many geological materials is a linear function of frequency (Turner and Siggins, 1994). Radar attenuation is closely related to the dielectric permittivity of earth materials. Dielectric permittivity is a frequency-dependent, complex quantity. Laboratory experiments (Lockner and Byerlee,

1985; Knight and Nur, 1987; Taherian et al., 1990) indicate that dielectric permittivity frequency dependence is a general phenomenon for most earth materials. Many theoretical models describe the frequency-dependent behavior of the dielectric permittivity, including the Debye model, which describes the dipolar response of the dielectric dispersion in a system with a single relaxation time, and the more commonly used Cole–Cole model, which describes a distribution of relaxation times (Cole and Cole, 1941; Davidson and Cole, 1951). Recently, Joncsher (1977, 1978) proposed a 'universal' power law function to describe the frequency dependence of the complex dielectric permittivity. The theoretical models and laboratory measurements suggest that the attenuation behavior of EM waves in materials with a low loss tangent is similar to the seismic case, with the bulk effect of the many contributing mechanisms to EM wave attenuation producing a linear frequency dependence. This phenomenon can be regarded as the constant Q model for EM waves (Turner and Siggins, 1994; Bano, 1996).

As a result of linear frequency dependence of attenuation, the spectrum centroid of a radar pulse experiences a downshift during propagation. The centroid downshift is proportional to the integral of an intrinsic attenuation coefficient with respect to length along the ray path. The CFDS approach can be used to analyze borehole radar data to tomographically reconstruct the attenuation distribution associated with lithologic and hydrogeologic features. The CFDS method is applicable to subsurface radar data in the MHz to GHz frequency range when the signal bandwidth is broad enough and the attenuation is high enough to cause noticeable losses of high frequencies during propagation.

3. The CFDS method

Assuming that the process of wave propagation can be described by linear system theory, if the amplitude spectrum of an incident wave is $S(f)$, and the medium and instrument response is $G(f)\cdot H(f)$, then the received amplitude spectrum $R(f)$ may be, in general, expressed as:

$$R(f) = G(f)\cdot H(f)\cdot S(f), \tag{6}$$

where the factor $G(f)$ includes geometric spreading, instrument response, source and receiver coupling to the medium, antenna radiation pattern, reflection and transmission coefficients, and the phase accumulation due to propagation, and $H(f)$ describes the attenuation effect on the amplitude. By adopting the constant Q model, the attenuation is then assumed to be proportional to frequency, that is to say $\alpha = \alpha_0 f$; here, α_0 may be regarded as an intrinsic attenuation coefficient. Then, the attenuation filter can be written as:

$$H(f) = \exp\left(-f\int_{\text{ray}} \alpha_0 \mathrm{d}l\right). \tag{7}$$

Our goal is to estimate medium response $H(f)$, or more specifically the attenuation coefficient α_0, from knowledge of the input spectrum $S(f)$ and the output spectrum $R(f)$. A direct approach is to solve Eq. (7) by taking the natural logarithm and obtaining:

$$\int_{\text{ray}} \alpha_0 \mathrm{d}l = \frac{1}{f}\ln\left[\frac{GS(f)}{R(f)}\right]. \tag{8}$$

Eq. (8) can be used to estimate the integrated attenuation at any frequency and could be called an amplitude-ratio method. However, the calculation of attenuation based on individual frequencies is not robust because of poor individual signal-to-noise ratio. The signal-to-noise ratio can be improved by averaging amplitudes over a range of frequencies, (Wright et al., 1996), but as described above, the factor G includes many complicated processes and is very difficult to determine. To overcome these difficulties, a statistically based method is used to estimate α_0 from the spectral centroid down-

shift over a range of frequencies. The centroid frequency of the input signal $S(f)$ is defined as:

$$f_S = \frac{\int_0^\infty f S(f)\,df}{\int_0^\infty S(f)\,df}, \tag{9}$$

and the variance is defined as:

$$\sigma_S^2 = \frac{\int_0^\infty (f - f_S)^2 S(f)\,df}{\int_0^\infty S(f)\,df}. \tag{10}$$

Similarly, the centroid frequency of the received signal $R(f)$ is:

$$f_R = \frac{\int_0^\infty f R(f)\,df}{\int_0^\infty R(f)\,df}, \tag{11}$$

and its variance:

$$\sigma_R^2 = \frac{\int_0^\infty (f - f_R)^2 R(f)\,df}{\int_0^\infty R(f)\,df}, \tag{12}$$

where $R(f)$ is given by Eq. (6). If G is independent of frequency f, then f_R and σ_R^2 will be independent of G. This is the major advantage of using the spectral centroid and variance rather than the actual amplitudes.

For the special case where the incident spectrum $S(f)$ is Gaussian, i.e.,

$$S(f) = \exp\left[-\frac{(f - f_S)^2}{2\sigma_S^2} \right]. \tag{13}$$

Substituting Eqs. (11) and (3) into Eq. (2), the centroid of the received signal (Quan and Harris, 1993, 1997) is given by:

$$f_R = f_S - \sigma_S^2 \int_{ray} \alpha_0\,dl, \tag{14}$$

and

$$A = G \exp\left(-\frac{f_d}{2\sigma_S^2} \right), \tag{15}$$

with

$$f_d = 2 f_S \sigma_S^2 \int_{ray} \alpha_0\,dl - \left(\sigma_S^2 \int_{ray} \alpha_0\,dl \right)^2, \tag{16}$$

where f_R is the centroid and A is the amplitude of $R(f)$. Eq. (14) states that the centroid of the spectrum of the received signal is downshifted in an amount that depends on the attenuation characteristics along the EM wave ray path. Eq. (15) states that the amplitude of the received signal is also dependent on the ray path attenuation characteristics, but in a more complicated manner. It is more straightforward to use the frequency downshift information (Eq. (14)) to construct the relation suitable for tomographic inversion. Eq. (14) can be rewritten as a line integral:

$$\int_{ray} \alpha_0\,dl = (f_S - f_R)/\sigma_S^2. \tag{17}$$

Under the assumption of a linear-dependence model of attenuation to frequency, a tomographic Eq. (17) has been derived for a Gaussian spectrum. The tomographic formula relating frequency shift with the attenuation projection is exact only for Gaussian spectra. Similar derivation can also be obtained for other frequency compositions such as rectangular and triangular spectra, but the equations are similar, which implies that the attenuation estimates are insensitive to small changes in spectrum shape. Eq. (17) shows that the attenuation coefficient for an inhomogeneous medium can be obtained by measuring the CFDS $(f_S - f_R)$ between the transmitted and received signals. The integrated attenuation equals this frequency downshift multiplied by a scaling factor. From Eq. (17), we can also see that for a certain value of α_0, a broader input bandwidth (larger σ_S) results in a larger frequency change. Therefore, a broad input frequency band is important for a robust estimation of α_0.

Eq. (17) is the basic formula for attenuation tomography. It can be written in discrete form:

$$\sum_j \alpha_{0j} l_j^i = \frac{f_S - f_R^i}{\sigma_S^2}, \tag{18}$$

where: i = the ith ray; j = the jth grid of the medium, and, l_j^i = the ray length within the jth grid.

In practice, one can measure f_R from recorded GPR profiles, but may not directly

measure the source centroid frequency f_S and the variance σ_S^2. For the linear model described by Eq. (3) and Gaussian spectrum given by Eq. (13), the source spectrum $S(f)$ and receiver spectrum $R(f)$ exhibit the same variance σ_S^2. Therefore, we may choose the average of variances σ_R^2 at the receivers to estimate the source variance σ_S^2. While the source spectral frequency f_S is also unknown, it can be assumed to be included along with the matrix of unknown attenuation values. Then, we can simultaneously invert for both the attenuation coefficients α_j and the source frequency f_S as follows. Let:

$$f_S = \bar{f}_S + \Delta f, \tag{19}$$

where $\bar{f}_S$ is the maximum of $\{f_R^i\}$ as an initial estimation of f_S, and Δf is a static correction. Then:

$$\frac{f_S - f_R^i}{\sigma_S^2} = \frac{\bar{f}_S + \Delta f - f_R^i}{\sigma_S^2} = \frac{\bar{f}_S - f_R^i}{\sigma_S^2} + \frac{\Delta f}{\sigma_S^2}. \tag{20}$$

Eq. (18) can be written as:

$$\sum_j \alpha_j l_j^i - \frac{\Delta f}{\sigma_S^2} = \frac{\bar{f}_S - f_R}{\sigma_S^2}, \tag{21}$$

where α_j and Δf are the unknowns.

Two commonly used approaches in inversion algorithm are the ART (Algebraic Reconstruction Technique) and the SIRT (Simultaneous Iterative Reconstruction Technique) methods (Lo and Inderwiesen, 1994). In this paper, the

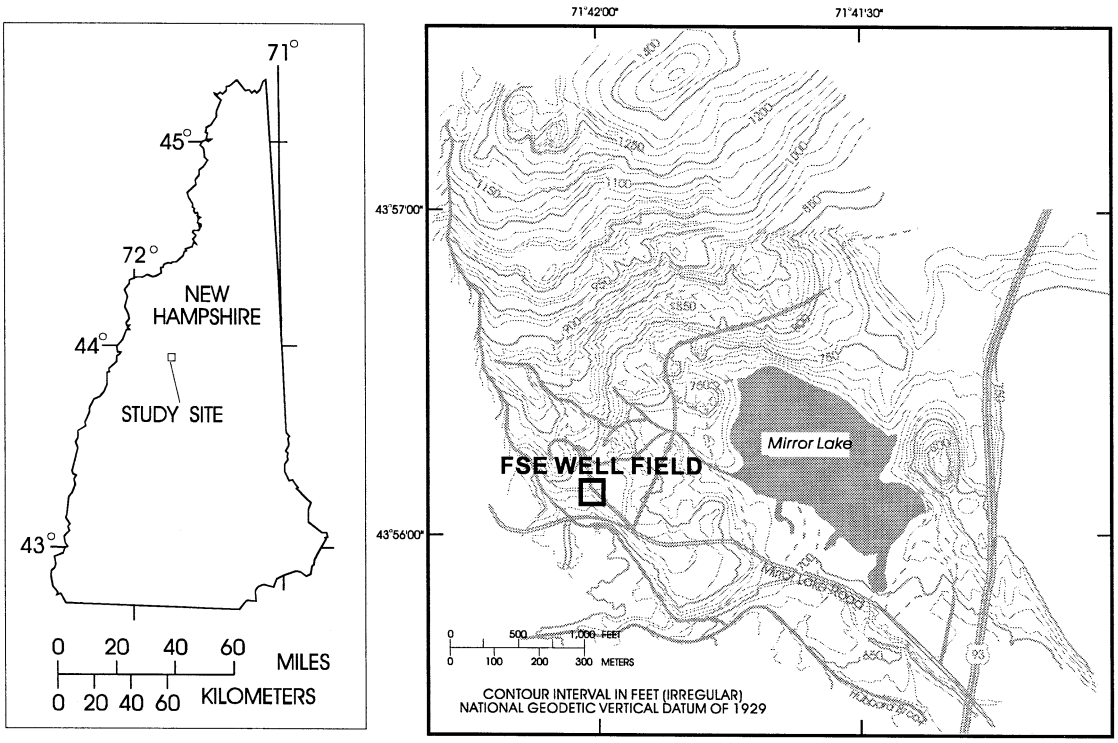

Fig. 1. Location of study area and the FSE well field at the U.S. Geological Survey Fractured Rock Research Site, Mirror Lake, Grafton County, NH. Left: the relative location of the study area in New Hampshire. Right: detailed site map with topography, the location of the Mirror Lake, and the FSE well field.

SIRT method was used to invert for the intrinsic attenuation coefficient.

4. Field experiment

The CDFS method was tested using cross-hole borehole radar data acquired at the U.S. Geological Survey Fractured Rock Research Site located in the U.S. Forest Service Hubbard Brook Experimental Forest in the Mirror Lake area near West Thornton, Grafton County, NH (Fig. 1). The experiment procedure is described by Lane et al. (1996) and Wright et al. (1996). Borehole radar surveys were conducted in a cluster of four boreholes, with each borehole at the corner of a square with a side length of about 9 m. The distance between the transmitting (FSE-3) and receiving (FSE-2) boreholes used for the experiment is about 12.96 m (Fig. 2).

The data used in this study were acquired in the summer of 1996. Using a RAMAC borehole radar system with 60-MHz antennas, the GPR data were acquired during a series of saltwater injection tests performed at this site for testing the ability of geophysical techniques to detect and monitor fluid flow in a fractured rock environment. During the tracer test, a hydraulically conductive zone connecting FSE-1 and FSE-4 was isolated using straddle packers. The isolated zone in FSE-4 was pumped at about 9 l/min while a NaCl solution with concentrations of 20 to 28 g/l was continuously injected into the packed-off interval between 42 and 49 m in FSE-1. To measure changes in wave attenuation due to the presence of tracer in the FSE-2 to FSE-3 plane, background and steady-state cross-hole tomography surveys were conducted between FSE-2 and FSE-3 with transmitter and receiver locations every 2 m from 19 to 71 m. A total of 729 rays were used for the inversion, with an approximate grid size of about 0.5×0.5 m.

Fig. 3 shows an example of the radar records collected (a) before and (b) during the saline-

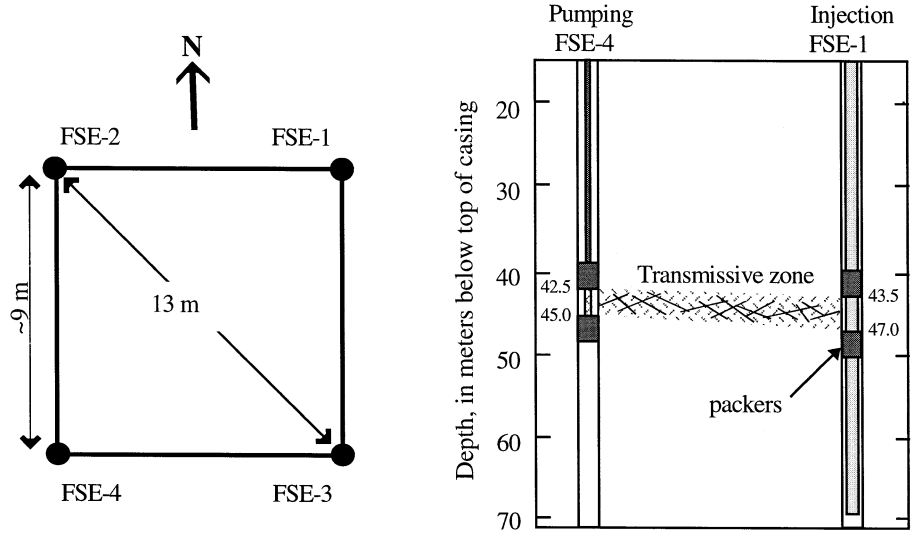

Fig. 2. The setup of the FSE well field. Left: the plan view of relative positions of boreholes for injection (FSE-1), pumping (FSE-4), and the cross-hole radar surveys (FSE-2 and FSE-3). The distances between FSE-3 (transmitting hole) and FSE-2 (receiving hole), and between FSE-1 (injection hole) and FSE-4 (pumping hole) are 13 m. Right: the hydrogeological cross-section between FSE-1 and FSE-4.

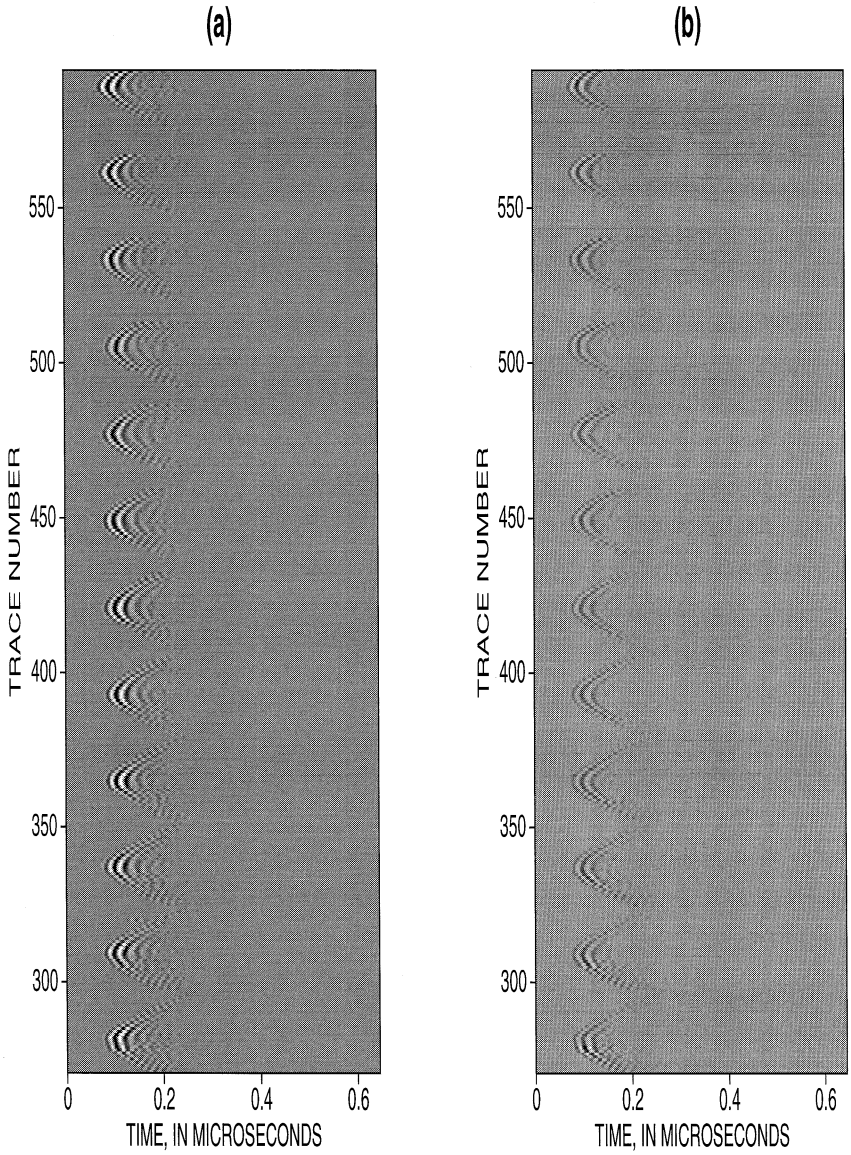

Fig. 3. A portion (324 traces) of the cross-hole radar records before [(a), left] and during [(b), right] saline-water injection recorded in boreholes, FSE-2 and FSE-3. The increased attenuation in the records during the injection test is expressed by lower amplitude (less contrast in this gray scale plot).

tracer injection test, showing a significant loss of amplitude in recorded data during injection, as compared to the background measurements. In Fig. 4, a histogram of frequency centroids for the background data and the data collected during injection is shown. The mean of the centroid frequency decreases about 2 MHz after injection, which is consistent with an increase in attenuation due to ray paths traversing regions containing the saline tracer. The downshift of the centroid frequency of a single ray may reach as high as 8 MHz (Fig. 5), more than one-tenth of the background centroid frequency of the 60-MHz antenna.

In Fig. 6, the attenuation tomograms from the ‘background’ (Fig. 6a) and ‘during injection’

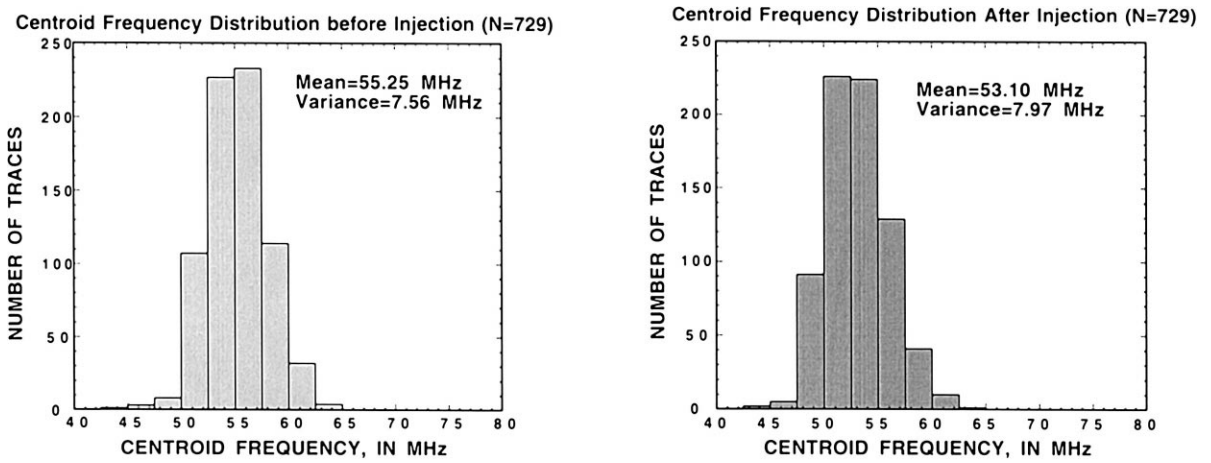

Fig. 4. Histograms for centroid frequency distribution for borehole radar data (729 traces in total). The mean of the centroid frequencies for data acquired before injection is 55.25 MHz, comparing with the nominal frequency of 60 MHz. Meanwhile, the mean of the centroid frequencies for data acquired during injection is 53.10 MHz. An average of 2.15 MHz downshift exists between the two means. This can be reasonably assumed as caused by the increase of salinity in the ground water during the injection test.

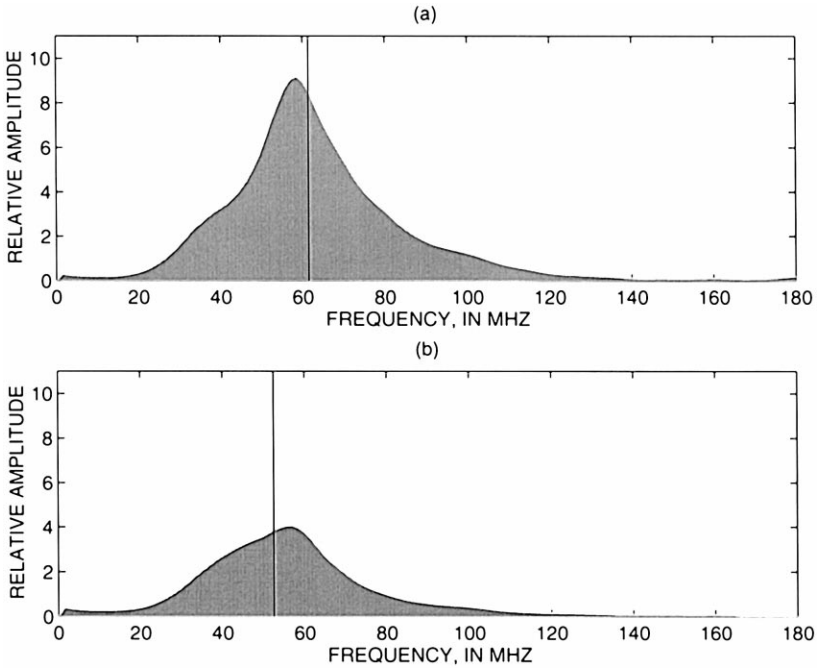

Fig. 5. An example of the downshift of the centroid frequency for a single trace (trace no. 691, with receiver at 49 m, and transmitter at 69 m below top of casing) when comparing the amplitude spectrum before injection with that of during the injection test. (a) Amplitude spectrum before injection, with the centroid (indicated by the vertical thin line) at 61.39 MHz. (b) Amplitude spectrum during the injection, with the centroid of the spectrum at 51.41 MHz.

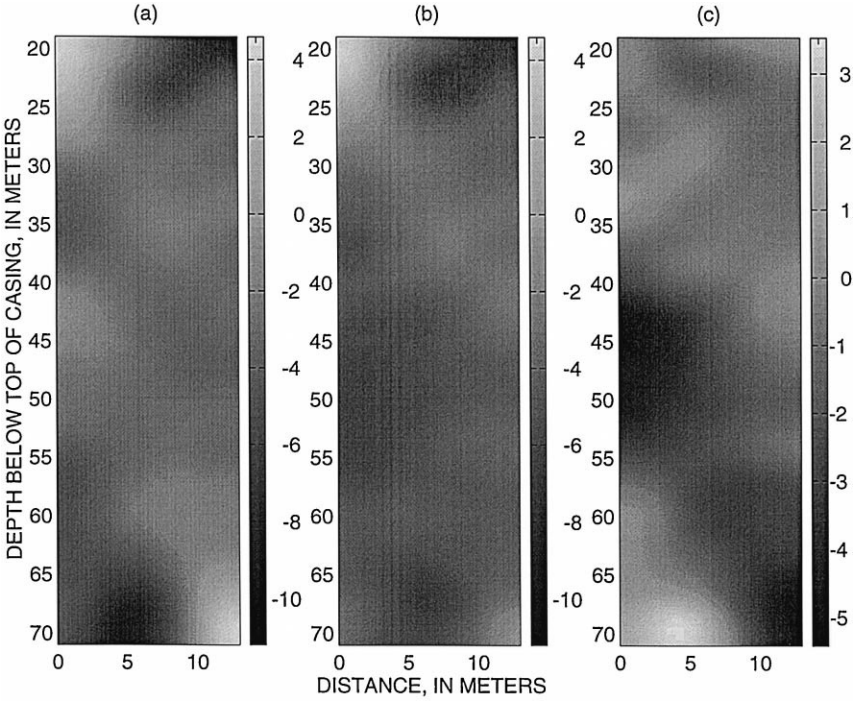

Fig. 6. Attenuation tomograms between FSE-2 and FSE-3 showing (a) the background before injection, (b) during injection, and (c) the differential attenuation. The attenuation is expressed using the intrinsic attenuation coefficient in the unit of 10 000 s-nepers/m. Darker color in gray scale indicates higher attenuation.

(Fig. 6b) surveys are shown along with the attenuation-difference tomogram (Fig. 6c) for the FSE-2 to FSE-3 plane. Because this plane is perpendicular to the injection-pumping plane (FSE-1 to FSE-4), high-attenuation zones should show the location and distribution of saline tracer in fractures as it crosses between FSE-2 and FSE-3. The highest attenuation occurs near the injection depths (40 m–50 m), close to borehole FSE-2. The attenuation pattern is consistent with a three-dimensional fracture network, with most of the tracer channelled along highly permeable fractures near FSE-2 that are well-connected to FSE-1 and FSE-4. Less permeable paths connecting FSE-1 and FSE-4 occur near FSE-3, and a permeable path connects the upper and lower hydraulically conductive zones (Fig. 2). The bright spots in the uppermost and lowermost corners may be due to the artifacts for improper ray coverage at edges. The increase of attenuation appears due to the elevated effective conductivity induced by the electrically conductive tracer. The attenuation-difference tomogram obtained by the frequency downshift method agrees with previous results (Lane et al., 1996; Wright et al., 1996).

5. Conclusions

Frequency-dependent attenuation causes a change in the amplitude distribution of a wave's frequency spectra. For a linear model and a Gaussian spectrum, this change is simple: the difference in centroid frequency between the incident (input) and transmitted (output) waves is proportional to the integrated attenuation multiplied by a scaling factor. The source frequency static correction introduced in this method makes the attenuation estimation robust and stable. CFDS analysis is relatively simple and is well-suited for attenuation and attenuation-difference

tomography. Although the CFDS method is sensitive to small frequency changes, it is best used on broadband data.

The CFDS method was applied to cross-hole radar data collected at the U.S. Geological Survey Fractured Rock Research Site in Mirror Lake, NH during a saline-tracer injection experiment. The attenuation-difference tomogram outlines the spatial distribution of the saline tracer in transmissive fractures that cross the tomographic image plane.

Acknowledgements

Lanbo Liu acknowledges the support of Schlumberger-Doll Research and the University of Connecticut Research Foundation. We are grateful to Dr. Feng Yin of Diasonics Ultrasound for his comments and discussions during preparing this manuscript. Constructive remarks and comments made by reviewers, Drs. John Greenhouse and Roger Roberts, and by co-editors, Profs. M. Sato and R. Versteeg greatly improved the manuscript. The authors would also like to acknowledge Peter Joesten (USGS) for preparing Figs. 1 and 2 and Alison Waxman (USGS) for careful editing the final draft of the manuscript.

References

Annan, A.P., 1996. Transmission dispersion and GPR. J. Environ. Eng. Geophys. 0, 125–136.

Balanis, C.A., 1989. Advanced Engineering Electromagnetics. Wiley, New York, 981 pp.

Bano, M., 1996. Constant dielectric losses of ground-penetrating radar waves. Geophys. J. Int. 124, 279–288.

Brewster, M.L., Annan, A.P., 1994. Ground-penetrating radar monitoring of a controlled DNAPL release: 200-MHz radar. Geophysics 59, 1211–1221.

Brewster, M.L., Annan, A.P., Greenhouse, J.P., Kueper, B.H., Olhoeft, G.R., Redman, J.D., Sander, K.A., 1995. Observed migration of a controlled DNAPL release by geophysical methods. Ground Water 33, 977–987.

Brzostowski, M., McMechan, G., 1992. 3-D tomographic imaging of near-surface seismic velocity and attenuation. Geophysics 57, 396–403.

Cole, K.S., Cole, R.H., 1941. Dispersion and absorption in dielectrics. J. Chem. Phys. 9, 341–351.

Daniels, J.J., Roberts, R., Vendl, M., 1995. Ground-penetrating radar for the detection of liquid contaminants. J. Appl. Geophys. 33, 195–207.

Davidson, D.H., Cole, R.H., 1951. Dielectric relaxation in glycerol, propylene glycol, and *n*-propanol. J. Chem. Phys. 29, 1484–1490.

Endres, A., Knight, R., 1991. The effects of pore-scale fluid distribution on the physical properties of partially saturated sandstones. J. Appl. Phys. 69, 1091–1098.

Endres, A., Redman, J.D., 1996. Modeling the electrical properties of porous rocks and soils containing immiscible contaminants. J. Environ. Eng. Geophys. 0, 105–112.

Feng, S., Sen, P.N., 1985. Geometrical model of conductive and dielectric properties of partially saturated rocks. J. Appl. Phys. 58, 3236–3243.

Greenhouse, J.P., 1992. Environmental geophysics. SEG Annual Meeting Expanded Technical Program Abstracts With Biographies 62, 603–609.

Greenhouse, J.P., Brewster, M., Schneider, G., Redman, D., Annan, P., Olhoeft, G., Lucius, J., Mazzella, A., 1993. Geophysics and solvents: the Borden experiment. The Leading Edge 12 (4), 261–267.

Greeuw, G., de Feijter, J.W., Kathage, A., 1992. Field and laboratory tests on line scatterers. Proceedings of the 4th International Conference on GPR, pp. 111–118.

Grumman, D.L., Daniels, J.J., 1996. Experiments on the detection of organic contaminants in the vadose zone. J. Environ. Eng. Geophys. 0, 31–38.

Joncsher, A.K., 1977. The ‘universal’ dielectric response. Nature 267, 673–679.

Joncsher, A.K., 1978. Low-frequency dispersion in carrier-dominant dielectrics. Philos. Mag. B 38, 587–601.

Kjartansson, E., 1979. Constant *Q*-wave propagation and attenuation. J. Geophys. Res. 84, 4137–4748.

Knight, R.J., Nur, A., 1987. The dielectric constant of sandstones, 60 kHz to 4 MHz. Geophysics 52, 644–654.

Lane, J.W., Haeni, F.P., Placzek, G., Wright, D., 1996. Use of borehole radar methods to detect a saline tracer in fractured crystalline bedrock at Mirror Lake, Grafton County, NH, USA. Proc. 6th Int. Conf. GPR, pp. 185–190.

Liu, L., Quan, Y., 1996. Subsurface radar wave attenuation tomography using the frequency shift method. Proc. 6th Int. Conf. GPR. Sendai, Japan, pp. 335–340.

Liu, L., Zhou, C., Lane, J.W., Haeni, F.P., 1997. Cross-hole radar attenuation tomography using a frequency centroid downshift method: consideration of non-linear frequency dependence of EM wave attenuation. Expanded abstract, 67th Annu. Int. Meeting, Soc. Exp. Geophys., 67: 422-425.

Lo, T.W., Inderwiesen, P., 1994. Fundamentals of Seismic Tomography. Society of Exploration Geophysicists, Tulsa, OK, 178 pp.

Lockner, D.A., Byerlee, J.D., 1985. Complex resistivity measurements of confined rock. J. Geophys. Res. 90, 7837–7847.

Quan, Y., Harris, J.M., 1993. Seismic attenuation tomography based on centroid frequency shift. Expanded Abstract of the 63rd SEG Annual Meeting. Washington, DC, pp. 41–44.

Quan, Y., Harris, J.M., 1997. Seismic attenuation tomography using the frequency shift method. Geophysics 62, 895–905.

Sato, M., Ohkubo, T., Niitsuma, H., 1995. Cross-polarization borehole radar measurements with a slot antenna. J. Appl. Geophys. 33, 53–61.

Sen, P.N., Scala, C., Cohen, M.H., 1981. A self-similar model for sedimentary rocks with application to the dielectric constant of fused glass beads. Geophysics 46, 781–795.

Sheriff, R.E., Geldart, L.P., 1995. Exploration Seismology. Cambridge Univ. Press, London, 592 pp.

Taherian, M.R., Kenyon, W.E., Safinya, K.A., 1990. Measurement of dielectric response of water-saturated rocks. Geophysics 55, 1530–1541.

Turner, G., Siggins, A.F., 1994. Constant *Q* attenuation of subsurface radar. Geophysics 59, 1192–1200.

Versteeg, R., Anderson, R., Boulanger, A., Xu, L., 1996. Four-dimensional visualization and analysis of GPR data for fluid flow estimation. SEG Annual Meeting Expanded Technical Program Abstracts with Biographies 66, 813–816.

Wright, D.L., Grover, T.P., Ellefson, K.J., Lane Jr., J.W., Kase, P.G., 1996. Radar tomograms at Mirror Lake, NH—3-D visualization and a brine injection experiment. In: Bell, R.S., Cramer, M.H. (Eds.), Proceedings of the Symposium on the Application of Geophysics to Engineering and Environmental Problems. Environmental and Engineering Geophysical Society. Keystone, CO, pp. 565–575.

Zucca, J.J., Hutchings, L.J., Kasameyer, P.W., 1994. Seismic velocity and attenuation structure of the Geysers geothermal field, California. Geothermics 23, 111–126.